

# GALACTIC OUTFLOWS BY ALFVÉNIC POYNTING FLUX: APPLICATION TO FERMI BUBBLES

TAKERU K. SUZUKI<sup>1,2</sup> & ALEX LAZARIAN<sup>3</sup>

*Draft version November 19, 2021*

## ABSTRACT

We investigate roles of magnetic activity in the Galactic bulge region in driving large-scale outflows of size  $\sim 10$  kpc. Magnetic buoyancy and breakups of channel flows formed by magnetorotational instability excite Poynting flux by the magnetic tension force. A three-dimensional global numerical simulation shows that the average luminosity of such Alfvénic Poynting flux is  $10^{40} - 10^{41}$  erg s<sup>-1</sup>. We examine the energy and momentum transfer from the Poynting flux to the gas by solving time-dependent hydrodynamical simulations with explicitly taking into account low-frequency Alfvénic waves of period of 0.5 Myr in a one-dimensional vertical magnetic flux tube. The Alfvénic waves propagate upward into the Galactic halo, and they are damped through the propagation along meandering magnetic field lines. If the turbulence is nearly trans-Alfvénic, the wave damping is significant, which leads to the formation of an upward propagating shock wave. At the shock front, the temperature  $\gtrsim 5 \times 10^6$  K, the density  $\approx 6 \times 10^{-4}$  cm<sup>-3</sup>, and the outflow velocity  $\approx 400 - 500$  km s<sup>-1</sup> at a height  $\approx 10$  kpc, which reasonably explain the basic physical properties of the thermal component of the Fermi bubbles.

*Subject headings:* accretion, accretion disks — Galaxy: bulge — Galaxy: center — magnetohydrodynamics (MHD) — turbulence – waves

## 1. INTRODUCTION

Large-scale outflows from the Galactic center (GC hereafter) region are observed in various wavelengths. Radio continuum observations identified the North Polar Spur (NPS hereafter), which extends above the Galactic latitude,  $b > 60$  degrees (Berkhuijsen et al. 1971). Although it might be interpreted by local supernova remnants (Berkhuijsen et al. 1971; Egger & Aschenbach 1995), Sofue (1977); Sofue & Handa (1984) claimed that this spur is linked to the GC. Later, large-scale bipolar structures were detected by X-ray observations (Snowden et al. 1997; Sofue 2000), although their origin was still vague. Bland-Hawthorn & Cohen (2003) finally identified bipolar structures and winds directly originating from the GC at the footpoint regions of these large-scale structures at mid-infrared wavelengths. Based on this observation, they further evaluated the energetics of the large-scale Galactic outflows from the GC in a quantitative sense, taking into account angular projection effect precisely (see Veilleux et al. 2005, for review).

Large-scale “haze” with the size of several kpc is also detected toward the GC in microwaves by WMAP (Finkbeiner 2004; Dobler & Finkbeiner 2008) and Planck (Planck Collaboration et al. 2013). Recently, the Fermi-LAT detected large-scale bipolar structures from the GC covering up to  $b \approx \pm 50$  degrees or  $\pm 10$  kpc (Dobler et al. 2010; Su et al. 2010), which are called Fermi bubbles. Emission mechanisms of the non-thermal  $\gamma$ -rays from the Fermi bubbles are discussed from hadronic (Crocker & Aharonian 2011; Fujita et al. 2013) and leptonic (Mertsch

& Sarkar 2011; Cheng et al. 2015) processes.

The origin of these bipolar structures is still under debate; a proposed mechanism is the past activity of the super-massive blackhole (SMBH hereafter) at the GC (Zubovas et al. 2011; Guo & Mathews 2012), which is inferred from X-ray observations (Koyama et al. 1996); another possibility is winds driven by multiple supernovae as a result of bursty star formation (Crocker 2012; Lacki 2014).

Quantitative properties of the Fermi bubbles have been known gradually to date. If the  $\gamma$ -rays are from the inverse Compton scattering by nonthermal electrons, following the leptonic scenario mentioned above, the magnetic field strength is constrained to be  $B = 5 - 20$   $\mu$ G from the synchrotron radiation of the same component of the electrons (Ackermann et al. 2014, see also Carretti et al. 2013). Kataoka et al. (2013, 2015) derived the temperature of the thermal gas in the bubbles is  $T \approx 3.5 \times 10^6$  K from spectral fitting to X-ray observations by *Suzaku*. From X-ray emission strengths of ionized oxygens, Miller & Bregman (2016) estimated  $T \approx (4 - 5) \times 10^6$  K and the density  $n \approx 1 \times 10^{-3}$  cm<sup>-3</sup> of the thermal component in the bubbles and the shells covering the bubbles. From these values, we can estimate the sound speed,

$$c_s = \sqrt{\frac{k_B T}{\mu m_p}} = 230 \text{ km s}^{-1} \left( \frac{T}{4 \times 10^6 \text{ K}} \right)^{1/2} \left( \frac{\mu}{0.6} \right)^{-1}, \quad (1)$$

and the Alfvén speed,

$$\begin{aligned} v_A &= \frac{B}{\sqrt{4\pi\mu m_p n}} \\ &= 890 \text{ km s}^{-1} \left( \frac{B}{10 \mu\text{G}} \right) \\ &\quad \left( \frac{n}{10^{-3} \text{ cm}^{-3}} \right)^{-1/2} \left( \frac{\mu}{0.6} \right)^{-1/2}, \quad (2) \end{aligned}$$

where  $k_B$  is the Boltzmann constant and  $m_p$  is the proton

arXiv:1710.03930v2 [astro-ph.GA] 19 Jan 2018

Electronic address: stakeru@ea.c.u-tokyo.ac.jp

<sup>1</sup> School of Arts & Sciences, the University of Tokyo, 3-8-1, Komaba, Meguro, Tokyo 153-8902, Japan;

<sup>2</sup> Department of Physics, Nagoya University, Furo-cho, Chikusa, Nagoya, Aichi 464-8602, Japan

<sup>3</sup> Department of Astronomy, University of Wisconsin-Madison, 2535 Sterling Hall, 475 North Charter Street, Madison, WI 53706-1507, USA

mass; we here assume the mean molecular weight  $\mu = 0.6$  as a standard value. From the comparison between Equations (1) and (2), the magnetic field is expected to affect the dynamics of the bipolar bubbles. Magnetohydrodynamical (MHD) simulations have been performed in order to examine roles of magnetic fields in driving bubbles/outflows (Barkov & Bosch-Ramon 2014; Mou et al. 2015).

One of the authors of the present paper also worked on a Global MHD simulation in the Galactic bulge region (Suzuki et al. 2015) and found that outflows are driven by the gradient of magneto-turbulent pressure and magnetic buoyancy (Parker instability; Parker 1966) in a stochastic manner (see also Machida et al. 2009, 2013). Because the main focus of Suzuki et al. (2015) was the generation of random velocities in the bulge, the simulation box covers up to the elevation angle of  $\pm 60$  degrees from the Galactic plane and cannot treat large-scale outflows. In the present paper, we carry out a pilot study how the Poynting flux generated from the Galactic Bulge heats up the Galactic halo and drives outflows, following the energy transfer in a one-dimensional (1D) flux tube by *time-dependent* simulations.

Breitschwerdt et al. (1991) introduced a theoretical framework for the galactic winds driven by the pressure of thermal gas, cosmic rays, and Alfvén waves under the *time-steady* approximation. This is further extended by explicitly taking into account specific interaction processes between these three components by Zirakashvili et al. (1996) and Ptuskin et al. (1997); in particular, they considered the excitation of Alfvén waves from cosmic rays via streaming instability (Wentzel 1968), and the dissipation of the excited Alfvén waves by nonlinear Landau damping (Kulsrud & Pearce 1969; Beresnyak & Lazarian 2008), which finally heats up the gas. The typical wavelength of the Alfvén waves is the gyroradius of relativistic ions,  $r_g \approx 3 \times 10^{11} \text{cm} \left(\frac{B}{10\mu\text{G}}\right)^{-1} \gamma$ , where  $\gamma$  is the Lorentz factor (Kulsrud & Pearce 1969; Everett et al. 2008). Namely the wavelength is shorter than the pc scale in general.

In the present paper, while we also consider Alfvénic Poynting flux, we present a model that is different from the previous works both in terms of the source of the Alfvénic waves and the damping mechanism. In particular, we consider the Poynting flux that is naturally produced by large-scale magnetic activity driven for example by magnetic loops and use the numerical simulations in Suzuki et al. (2015) for our quantitative studies. The typical wavelength of these Alfvénic waves is  $\sim 0.1 - 1$  kpc. Such long-wavelength Alfvénic waves hardly suffer nonlinear Landau damping. Therefore, we cannot assume instantaneous dissipation of the Alfvén waves, which is often adopted (e.g., Everett et al. 2008). Instead, we explicitly treat the transfer of the Alfvénic Poynting flux. For the damping of Alfvénic waves we use models of turbulent damping of Alfvénic waves (Yan & Lazarian 2002; Farmer & Goldreich 2004; Lazarian 2016). In these models MHD turbulence efficiently cascades Alfvén waves in the MHD regime, independently of the plasma parameters of the media, but depending on the level of background turbulence.

It is a key to properly model the damping rate of the

Alfvénic waves and to calculate both heating and wind launching by the wave damping in a self-consistent manner. If Alfvénic waves are damped near the Galactic bulge where the density is high, the final wind velocity is considered to be not fast enough to escape from the Galaxy. This is first because the momentum injection near the wind base does not launch an outflow, but lifts up the gas by contributing to the pressure balance, and second because the energy injection in the high-density region is mainly lost by radiation cooling and does not lead to a substantial increase of the temperature. On the other hand, wave dissipation at high latitudes is expected to drive the wind and the velocity of the wind depends on the density where the wave dissipation mainly happens. In addition, heating in rarefied gas can significantly increase the temperature due both to lower mass to be heated and lower cooling efficiency.

Our focus is on the thermal component of the bipolar bubbles and outflows. Here we briefly describe the global energetics, following Miller & Bregman (2016), in which each bubble is modeled by a simple prolate ellipsoid with semi-major axis = 5 kpc and semi-minor axis = 3 kpc. The total energy in one bubble is

$$E_{\text{th}} = \frac{k_B T}{\mu m_p} M_{\text{th}} = 5.9 \times 10^{54} \text{erg} \left(\frac{T}{4 \times 10^6 \text{K}}\right) \left(\frac{\mu}{0.6}\right)^{-1} \left(\frac{M_{\text{th}}}{5.4 \times 10^6 M_\odot}\right), \quad (3)$$

where  $M_{\text{th}}$  is the mass of the thermal component in one bubble. If we know the duration,  $\tau_{\text{inj}}$ , of the energy injection from the bulge, we can estimate the minimum required energy injection rate to keep  $E_{\text{th}}$ :

$$L_{\text{inj}} = \frac{E_{\text{th}}}{\tau_{\text{inj}}} = 1.9 \times 10^{40} \text{erg s}^{-1} \left(\frac{E_{\text{th}}}{5.9 \times 10^{54} \text{erg}}\right) \left(\frac{\tau_{\text{inj}}}{10 \text{Myr}}\right)^{-1}. \quad (4)$$

We should note that  $\tau_{\text{inj}}$  is very uncertain and the adopted value in previous works varies from a few  $10^5$  Myr (e.g. Guo & Mathews 2012) to  $\gtrsim$  a few  $10^8$  Myr (e.g. Crocker et al. 2015) in different theoretical models, whereas too long  $\tau_{\text{inj}} \gg$  a few Myr may be unrealistic (Bland-Hawthorn et al. 2013). Therefore, we leave  $\tau_{\text{inj}}$  as a free parameter in our model calculations (Section 3).

In Section 2, we briefly summarize the global 3D MHD simulation by Suzuki et al. (2015) and examine the Poynting flux ejected from the bulge region in the numerical data. In Section 3, we introduce our model to cover a large vertical region. We present main results in Section 4 and discuss related topics in Section 5

## 2. INJECTION OF ALFVÉNIC FLUX FROM THE GALACTIC BULGE

In this section we briefly describe the global MHD simulation in Suzuki et al. (2015) and quantify the up-going Poynting flux derived from the simulation, which will contribute to the heating and driving outflows in the Galactic halo region. The simulation was carried out in spherical coordinates,  $(r, \theta, \phi)$ , and covers a wide radial region from the inner radius at 0.01 kpc to the

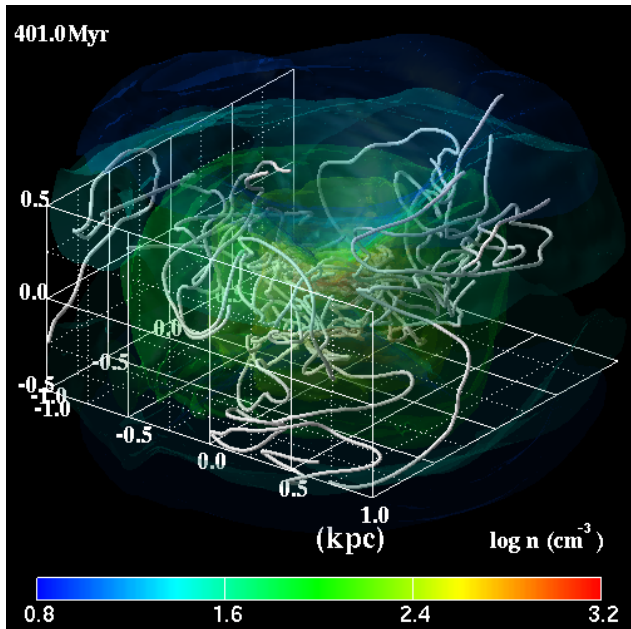


FIG. 1.— Snapshot view of magnetic field lines (white lines) and density contour (transparent colors) at  $t = 401.0$  Myr after the simulation (Suzuki et al. 2015) sets in.

outer boundary at 60 kpc. On the other hand, it covers  $30^\circ \leq \theta \leq 150^\circ$  ( $\pm 60^\circ$  degrees from the Galactic plane) and does not treat bipolar outflows ejected from the bulge region.

The simulation started from a very weak vertical magnetic field with  $0.7 - 20 \mu\text{G}$  in the bulge region. Magnetorotational instability (Velikhov 1959; Chandrasekhar 1961; Balbus & Hawley 1991, MRI hereafter) triggers the amplification of the magnetic field by creating the radial component in high- $\beta$  regions where the gas pressure dominates the magnetic pressure. At higher altitudes in which the magnetic pressure is comparable to or exceeds the gas pressure, Parker instability (Parker 1966) also amplifies horizontal magnetic field to further create the vertical component and excites vertical flows. The radial differential rotation and vertical shear also amplify the magnetic field efficiently by field-line stretching (see also Vishniac & Cho 2001; Vishniac & Shapovalov 2014, for Galactic dynamo).

Figure 1 presents a snapshot of magnetic field lines and density structure taken from Suzuki et al. (2015)<sup>4</sup>, which shows entangled turbulent field lines. When the quasi-saturated state is achieved after  $t \gtrsim 300$  Myr, the average field strength in the bulge region is  $0.1 - 1$  mG and it exceeds mG in local regions with field concentration, which are consistent with the lower limit  $> 50 \mu\text{G}$  from  $\gamma$ -ray observations (Crocker et al. 2010) and an estimated value,  $\approx$  a few mG, in a dense cloud (Pillai et al. 2015) based on the Chandrasekhar & Fermi (1953) method.

Although Suzuki et al. (2015) discussed outflows from the bulge region, they did not examine the outgoing

<sup>4</sup> Suzuki et al. (2015) made a mistake when converting the nondimensional units used for the simulation to the physical units, and the time unit must be smaller by  $\approx 10\%$ . Suzuki et al. (2015) presents a snapshot at  $t = 439.02$  Myr, but this time must be corrected to be  $t = 401.0$  Myr as shown in Figure 1.

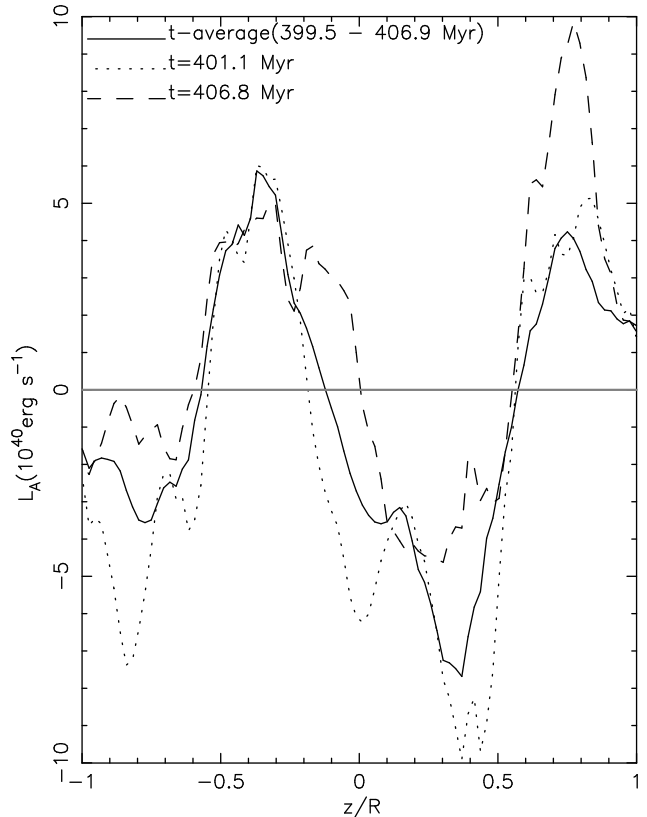


FIG. 2.— Alfvénic luminosity,  $L_A$ , integrated from  $R_{\text{in}} (= 0.23$  kpc) to  $R_{\text{out}} (= 1.1$  kpc) as a function of  $z/R$ .  $L_A$  averaged during time = 399.5 – 406.9 Myr (solid line) is compared to snapshots at 401.1 Myr (dotted line) and 406.8 Myr (dashed line).

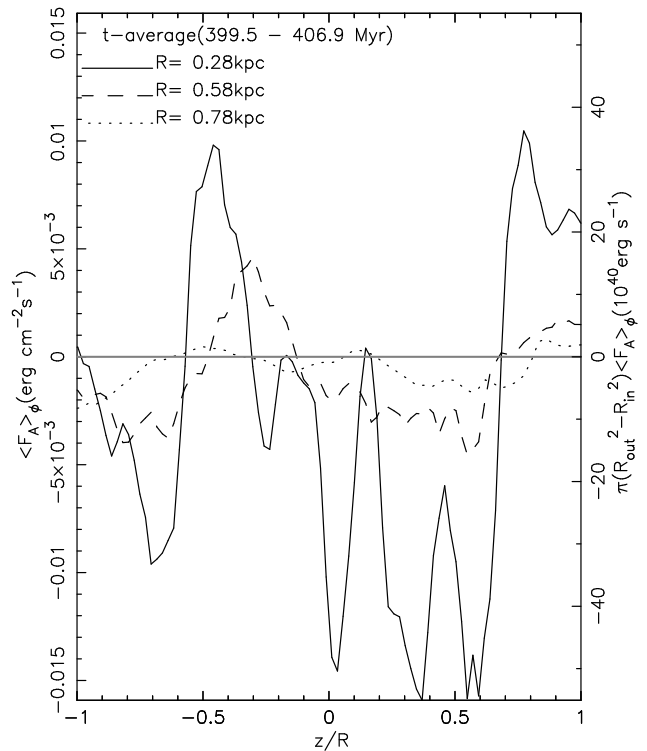


FIG. 3.— Alfvénic energy flux averaged over time and azimuthal angle at different  $R = 0.28$  kpc (solid),  $0.58$  kpc (dashed), and  $0.78$  kpc (dotted).

Poynting flux. In order to connect to the 1D vertical flux tube we model in Section 3, we analyze the Poynting flux of the simulation data in the cylindrical coordinates,  $(R, \phi, z)$ . The vertical ( $z$ ) component of Poynting flux in the MHD approximation (see also Equation A2) can be reduced to

$$-\left[\frac{1}{4\pi}(\mathbf{v} \times \mathbf{B}) \times \mathbf{B}\right]_z = \frac{1}{4\pi} (v_z \mathbf{B}_\perp^2 - B_z \mathbf{v}_\perp \cdot \mathbf{B}_\perp), \quad (5)$$

where the subscript  $\perp$  indicates the two perpendicular ( $R$  and  $\phi$ ) components with respect to the  $z$  direction; the first term corresponds to the Poynting flux carried by advected magnetic energy and the second term denotes the Poynting flux by magnetic tension force. If we examine this second term, we can estimate the net upgoing energy flux of Alfvénic perturbations.

In order to compare the energetics argument shown in Equation (4), we take the areal integration of the Alfvénic Poynting flux carried by MHD plasma along the  $z$  direction<sup>5</sup>,

$$F_A = -\frac{1}{4\pi} B_z \mathbf{v}_\perp \cdot \mathbf{B}_\perp, \quad (6)$$

to derive ‘‘Alfvénic luminosity’’,

$$L_A(z/R) = \int_0^{2\pi} d\phi \int_{R_{\text{in}}}^{R_{\text{out}}} R dR [F_A]_{z/R}, \quad (7)$$

where  $F_A$  is positive ( $\mathbf{v}_\perp \cdot \mathbf{B}_\perp < 0$ ) when flux is directed to  $+B_z$ , and we adopt  $R_{\text{in}} = 0.23$  kpc and  $R_{\text{out}} = 1.1$  kpc to cover the bulge region. We do not take the inner boundary = 0.01 kpc of the simulation for  $R_{\text{in}}$  because we would like to avoid unphysical effects of the boundary. For the radial integration, we take Poynting flux at the same aspect ratio,  $z/R$ , instead of the same height,  $z$ , because the simulation, which was carried out in spherical coordinates, do not have data in the region with large  $z$  at small  $R$ .

Figure 2 shows the vertical profile of  $L_A$ . We note that the vertical boundaries of the 3D simulation by Suzuki et al. (2015) are located at  $z/R = 1.4$ , and we do not consider the effect of the boundaries is sever in the plotting region,  $|z/R| \leq 1$ . One may recognize a characteristic feature in the plot: The direction of  $L_A$  is toward the Galactic plane in  $|z/R| \lesssim 0.6$ ; on the contrary it is directed upward (+ for  $z/R > 0$  and  $-$  for  $z/R < 0$ ) in  $|z/R| \gtrsim 0.6$ . This indicates that Alfvénic Poynting flux is injected from the regions at  $|z/H| \approx 0.6$  toward both midplane and upper directions. This behavior is already observed in local shearing box (Suzuki & Inutsuka 2009) and global (Suzuki & Inutsuka 2014) simulations, and these regions are called injection regions. While the magnetic energy is dominated by the thermal energy (plasma  $\beta \gg 1$ ) below the injection regions ( $|z/R| \lesssim 0.6$ ), the magnetic energy is comparable to the thermal energy ( $\beta \approx 1$ ) above the injection regions ( $z/R \gtrsim 0.6$ ). As a result, large-scale channel-mode flows are developed by the MRI near the injection regions, and breakups of these channel flows drive flows and Poynting fluxes to the lower and upper directions.

<sup>5</sup> Here we assume the background is static. A general expression for the energy flux of Alfvénic waves can be found in Equation (A5) in Appendix.

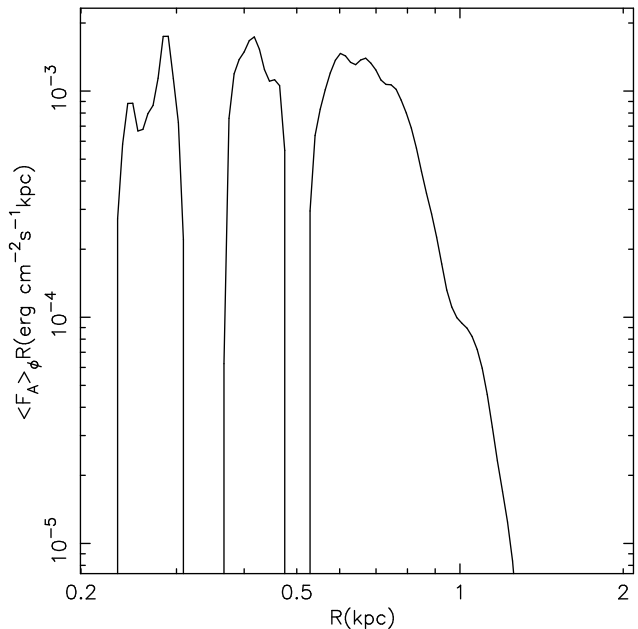


FIG. 4.— Radial dependence of Alfvénic energy flux multiplied by  $R$  kpc averaged over time, azimuthal angle, and  $0.75 < |z/R| < 0.9$ .

The time-averaged  $L_A$  during a period of 7.4 Myr (solid line in Figure 2) reaches  $\approx 4 \times 10^{40} \text{ erg s}^{-1}$  at  $|z/H| \approx 0.8$ , which is comparable to the estimate in Equation (4).  $L_A$  at two snapshots (dotted and dashed lines) show that  $L_A$  fluctuates with time and sometimes becomes  $\sim 10^{41} \text{ erg s}^{-1}$ .

In order to examine spacial fluctuations of Alfvénic flux, we plot the energy flux averaged during 7.4 Myr over the full  $2\pi$  azimuthal angle,

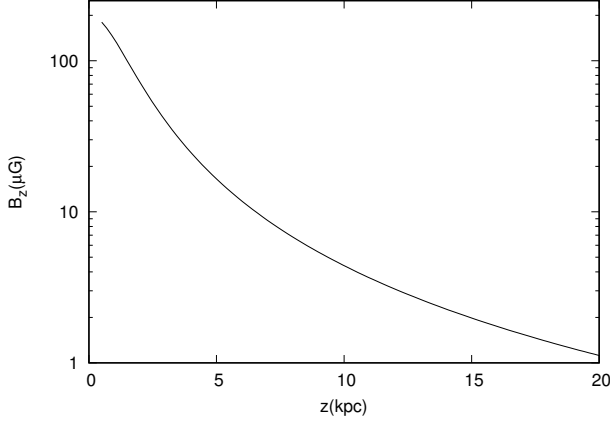
$$\langle F_A \rangle_\phi = \int_0^{2\pi} d\phi F_A / 2\pi, \quad (8)$$

at different rings,  $R = 0.28, 0.58,$  and  $0.78$  kpc in Figure 3. On the right axis, we show  $\langle F_A \rangle_\phi$  multiplied by the bulge area  $\pi(R_{\text{out}}^2 - R_{\text{in}}^2)$  to give the unit of luminosity, which can be directly compared to Figure 2. These three locations give the similar trend with the injection regions around  $|z/R| \approx 0.5 - 0.8$ , which was shown in Figure 2. On the other hand, the energy flux is larger at inner locations, and at  $R = 0.28$  kpc  $\langle F_A \rangle_\phi \pi(R_{\text{out}}^2 - R_{\text{in}}^2)$  is nearly  $4 \times 10^{41} \text{ erg s}^{-1}$ , which is  $\approx 10$  times larger than the time-averaged  $L_A$  in Figure 2.

Figure 4 presents the radial dependence of Alfvénic Poynting flux. We take the average in a region of  $0.75 < |z/R| < 0.9$ , which is located above the injection region and show  $\langle F_A \rangle_\phi R \text{ erg cm}^{-2} \text{ s}^{-1} \text{ kpc}$  to see the contribution to luminosity, Equation (7). This plot shows that the Alfvénic Poynting flux equally contributes to the luminosity in most of the bulge region,  $R_{\text{in}} < R < R_{\text{out}}$  except for a few regions ( $R \approx 0.25$  and  $0.5$  kpc) that temporally give negative  $F_A$ .

### 3. MODEL FOR ALFVÉNIC WAVE-DRIVEN OUTFLOWS

We consider the generation of outflows driven by low-frequency Alfvénic waves in a 1D flux tube that extends to the vertical direction,  $z$ . We assume the cross section


 FIG. 5.— Vertical profile of  $B_z$ .

of the flux tube expands with  $z$  in the following manner (Kopp & Holzer 1976; Breitschwerdt et al. 1991; Everett et al. 2008):

$$A = A_{\text{mid}} \left[ 1 + \left( \frac{z}{z_{\text{break}}} \right)^2 \right], \quad (9)$$

where  $A = A_{\text{mid}}$  at the Galactic midplane,  $z = 0$ . In this functional form the cross section is almost constant in  $z < z_{\text{break}}$ , and after that it expands with  $\propto z^2$  in a spherical manner at a large distance,  $z > z_{\text{break}}$  in the Galactic halo.

We consider a 1D magnetic flux tube located at  $R = R_0 = 0.3$  kpc, which is slightly offset from the GC, whereas the choice of  $R_0$  does not affect our results unless we choose a large  $R_0 > 1$  kpc. The magnetic flux tube, which is fixed with time, is set up to follow Equation (9). The conservation of magnetic flux,  $\nabla \cdot \mathbf{B} = 0$  gives

$$B_z = B_{\text{mid}} A_{\text{mid}} / A, \quad (10)$$

We assume  $B_{\text{mid}} = 200 \mu\text{G}$  at  $z = 0$  and  $z_{\text{break}} = 1.5$  kpc. These choices give the profile of  $B_z$  as shown in Figure 5, which is consistent with the observationally constrained magnetic field strength, 5-20  $\mu\text{G}$ , in the Fermi bubbles (Ackermann et al. 2014).

We follow the time evolution of mass density,  $\rho$ , vertical velocity,  $v_z$ , and internal energy of gas,  $e_g$ , in this geometry of flux tubes by our 2nd order Godunov method (Sano et al. 1999). The equation of mass conservation in the Lagrangian form is

$$\frac{d\rho}{dt} + \frac{\rho}{A} \frac{\partial}{\partial z} (A v_z) = 0. \quad (11)$$

The momentum equation is

$$\rho \frac{dv_z}{dt} = -\frac{\partial}{\partial z} (p_g + p_A) - \rho \frac{\partial \Phi}{\partial z} = 0, \quad (12)$$

where  $p_g$  is gas pressure,  $p_A$  is pressure of Alfvénic waves, which is modeled below, and  $\Phi$  is a gravitational potential. The internal energy of gas is related to gas pressure and temperature via

$$e_g = \frac{1}{\gamma - 1} \frac{p_g}{\rho} = \frac{1}{\gamma - 1} \frac{k_B T}{\mu m_p}, \quad (13)$$

where the ratio of specific heats is assumed to be  $\gamma = 5/3$ . The energy equation that determines  $e_g$  is

$$\rho \frac{de_g}{dt} + \frac{p_g}{A} \frac{\partial}{\partial z} (A v_z) = H_A \quad (14)$$

where  $H_A$  indicates the heating by the dissipation of Alfvénic waves, which is modeled below. In Equation (14), we do not take into account radiative cooling, because its contribution is not substantial (Everett et al. 2008).

We handle the propagation and dissipation of Alfvénic waves by the WKB approximation (Belcher 1971; Alazraki & Couturier 1971; Lamers & Cassinelli 1999); instead of directly solving MHD wave equations, we follow the variation of wave amplitude as a function of  $t$  and  $z$ . The amplitudes of velocity and magnetic fields of Alfvénic perturbations are related via

$$\mathbf{v}_\perp = -\frac{\mathbf{B}_\perp}{\sqrt{4\pi\rho}}. \quad (15)$$

Based on this relation, we define energy per mass,  $e_A$ :

$$e_A \equiv \frac{1}{2} \mathbf{v}_\perp^2 + \frac{\mathbf{B}_\perp^2}{8\pi\rho} = \mathbf{v}_\perp^2 = \frac{\mathbf{B}_\perp^2}{4\pi\rho}. \quad (16)$$

We consider Alfvénic waves in a frequency range from  $\omega_0$  to  $\omega_1$ ,

$$e_A = \int_{\omega_0}^{\omega_1} d\omega \tilde{e}_A(\omega) d\omega = \int_{\omega_0}^{\omega_1} d\omega \tilde{e}_A(\omega_0) f(\omega/\omega_0) d\omega, \quad (17)$$

where we assume a power-law-dependence on frequency,  $\omega$ ,

$$f(\omega/\omega_0) = \left( \frac{\omega}{\omega_0} \right)^{-\alpha}. \quad (18)$$

We do not assume a wide-band spectrum but a rather narrow-band spectrum within a range of an order of magnitude between  $\omega_0$  and  $\omega_1$ , which is expected from magnetic activity with the characteristic timescale  $\sim 0.1 - 1$  Myr (see below for the specific choices of  $\omega_0$ ,  $\omega_1$ , and  $\alpha$ ).

Assuming Alfvénic waves that propagate along the  $+B_z$  direction and the wavelengths are shorter than a typical scale, e.g. a pressure scale height or a variation scale of Alfvén speed, of the background physical properties, we can derive an equation that describes the variation of  $\tilde{e}_A$  (see Appendix for the detailed derivation):

$$\rho \frac{d\tilde{e}_A}{dt} + \frac{1}{A} \frac{\partial}{\partial z} \left[ A \rho \tilde{e}_A \left( v_A + \frac{1}{2} v_z \right) \right] - \frac{v_z}{2} \frac{\partial}{\partial z} (\rho \tilde{e}_A) = -\gamma_A \rho \tilde{e}_A, \quad (19)$$

where  $v_A = B_z / \sqrt{4\pi\rho}$ ,  $\gamma_A$  is the damping rate of Alfvénic waves, and we neglect nonlinear interactions between different waves and assume that waves with different frequencies evolve independently. In this case, we can derive an equation that describes the evolution of the spectral index (see Appendix):

$$\frac{d\alpha}{dt} + v_A \frac{\partial \alpha}{\partial z} = \frac{\gamma_A(\omega) - \gamma_A(\omega_0)}{\ln(\omega/\omega_0)}. \quad (20)$$

For the wave component, we solve Equation (19) for  $\omega = \omega_0$  and Equation (20), and then, we can derive the energy density,  $e_A$ , integrated over  $\omega$  from Equation (17). The

heating rate by the dissipation of Alfvénic waves (Equation 14) can be derived from the frequency-integrated damping rate,

$$H_A = \langle \gamma_A \rho e_A \rangle = \int_{\omega_0}^{\omega_1} d\omega \gamma_A(\omega) \rho \tilde{e}_A(\omega). \quad (21)$$

The gravitational potential,  $\Phi$ , in Equation (12) consists of four components,

$$\Phi = \sum_{i=1}^4 \Phi_i, \quad (22)$$

where each component corresponds to the SMBH at the Galactic center ( $i = 1$ ), the bulge ( $i = 2$ ), the disk ( $i = 3$ ), and the dark halo ( $i = 4$ ). For the SMBH, we adopt a point-mass,  $M_1 = 4.4 \times 10^6 M_\odot$ , at the GC (Genzel et al. 2010), where  $M_\odot$  is the solar mass. For the bulge and disk components, we use a gravitational potential introduced by Miyamoto & Nagai (1975):

$$\Phi_{i=2,3}(R, z) = \frac{-GM_i}{\sqrt{R^2 + (a_i + \sqrt{b_i^2 + z^2})^2}}, \quad (23)$$

where  $M_2 = 2.05 \times 10^{10} M_\odot$ ,  $a_2 = 0$ ,  $b_2 = 0.495$  kpc,  $M_3 = 25.47 \times 10^{10} M_\odot$ ,  $a_3 = 7.258$  kpc, and  $b_3 = 0.52$  kpc. For the dark halo, we adopt the NFW density profile (Navarro et al. 1996), which gives the following form of the gravitational potential (e.g., Kuzio de Naray et al. 2009),

$$\Phi_4 = -4\pi G \rho_{h,0} r_h^3 \frac{1 + r/r_h}{r}, \quad (24)$$

where  $r = \sqrt{R^2 + z^2}$  is the spherical radius, and we assume  $r_h = 10.7$  kpc and  $\rho_{h,0} = 1.82 \times 10^{-2} M_\odot \text{pc}^{-3}$  (Sofue 2015).

Alfvénic perturbations injected by the magnetic activity in the Galactic bulge region travel upward into the Galactic halo. We focus on low-frequency Alfvénic waves with the typical wavelength 0.1 – 1 kpc. Such long-wavelength waves are not subject to nonlinear Landau damping, which is effective for waves with the wavelength of an order of the gyration scale (Kulsrud & Pearce 1969; Beresnyak & Lazarian 2008, see also Section 1). We also restrict our focus on linear Alfvén waves, of which the amplitude is significantly smaller than the local Alfvén speed. Such linear waves in the MHD regime do not suffer dissipation in homogeneous media. However, if the background magnetic medium is turbulent, Alfvén waves are damped because of the meandering magnetic field (Lazarian 2016). Indeed, various sources of turbulence in the Fermi bubbles have been proposed, such as Kelvin-Helmholtz, Rayleigh-Taylor, or Richtmyer-Meshkov instabilities behind shock fronts (Guo & Mathews 2012; Inoue 2012; Sasaki et al. 2015), and infalling stars and gas clouds to the central SMBH (Cheng et al. 2015).

We consider MHD turbulence injected from large-scale sources with size  $\sim 1$  kpc. The linear damping rate of Alfvén waves can be found in Lazarian (2016):

$$\gamma_A = \frac{v_A M_A^{4/3} \sin^{2/3} \theta}{L^{1/3} \lambda^{2/3}} \approx \frac{v_A M_A^2}{L^{1/3} \lambda^{2/3}} = \frac{v_A M_A^2 \omega^{2/3}}{L^{1/3} (v_A + v_z)^{2/3}}, \quad (25)$$

where  $L$  is an injection scale of turbulence,

$$\lambda = (v_A + v_z) \tau_w = (v_A + v_z) \left( \frac{2\pi}{\omega} \right) \quad (26)$$

is the wavelength of propagating waves,  $M_A$  is the Mach number of turbulence, and  $\theta$  is the angle between the direction of the wave propagation and the background magnetic field. We focus on the Alfvén waves that propagate in parallel with the average direction of the background field; in this case the angle  $\theta$  can be approximated by the meandering angle of magnetic field lines,

$$\sin \theta \approx \delta B / B_z = M_A, \quad (27)$$

where  $\delta B$  is the amplitude of magnetic turbulence. When deriving the final approximate expression of Equation (25), we used Equation (27).

We consider large-scale sources for the turbulence as discussed above, and assume  $L = 1$  kpc in this paper. Wave sources are various magnetic activities in the bulge regions, such as breakups of channel flows, buoyantly rising magnetic loops (Fukui et al. 2006; Torii et al. 2010b,a), and spring-like helical magnetic structure (Enokiya et al. 2014). For rough estimates, let us consider magnetic structure with field strength of  $B \sim 300 \mu\text{G}$  and a size of  $l_B \sim 0.1$  kpc, which generates Alfvénic Poynting flux. Then, we get a characteristic period,

$$\begin{aligned} \tau_w &\sim l_B / v_A \\ &\approx 0.3 \text{ Myr} \left( \frac{l_B}{0.1 \text{ kpc}} \right) \left( \frac{B}{300 \mu\text{G}} \right)^{-1} \left( \frac{n}{10 \text{ cm}^{-3}} \right)^{1/2} \end{aligned} \quad (28)$$

Following the above estimate, we consider waves in a range between  $\tau_{w,1} = 0.1$  Myr and  $\tau_{w,0} = 1$  Myr, and inject Alfvénic waves in  $\omega_0 < \omega < \omega_1$  with a power-law index,  $\alpha = 1$ , where  $\omega_0 = 2\pi/\tau_{w,0}$  and  $\omega_1 = 2\pi/\tau_{w,1}$ . Note that  $\alpha = 1$  indicates that waves with different  $\omega$  are equally injected in logarithmic spacing,  $d \log \omega$ . We leave the uncertainty of the wave damping to  $M_A$ ; choosing a smaller  $L$  is practically the same as setting a larger  $M_A$ . We analyze the effect of the wave damping by changing  $M_A$ .

For later analyses, we would like to estimate a typical wavelength:

$$\lambda \sim v_A \tau_w \approx 0.3 \text{ kpc} \left( \frac{v_A}{1000 \text{ km s}^{-1}} \right) \left( \frac{\tau_w}{0.3 \text{ Myr}} \right), \quad (29)$$

where we neglect  $v_z$  in Equation (26) and adopt a standard value for the Alfvén speed in the halo region.

The calculation region covers from the bottom boundary at  $z = 0.5$  kpc to the top boundary = 23 kpc. Initially we set up the hydrostatic equilibrium with a constant temperature,  $T_{\text{halo}} = 2 \times 10^6$  K, in the Galactic halo (Miller & Bregman 2016). At the bottom boundary at  $z = 0.5$  kpc, we set the particle number density  $n = 4.5 \times 10^{-1} \text{ cm}^{-3}$ , which corresponds to the electron number density  $\approx 2.4 \times 10^{-1} \text{ cm}^{-3}$  for  $\mu = 0.6$ . The hydrostatic density structure gives  $n = 1.9 \times 10^{-4} \text{ cm}^{-3}$  at  $z = 10$  kpc. We note that the density shown in Figure 1 is  $n \approx 10 \text{ cm}^{-3}$  at  $z = 0.5$  kpc, which is larger than the density adopted at the bottom boundary of the present setup. This is because of the difference of the adopted temperatures. In the 3D simulation of Figure

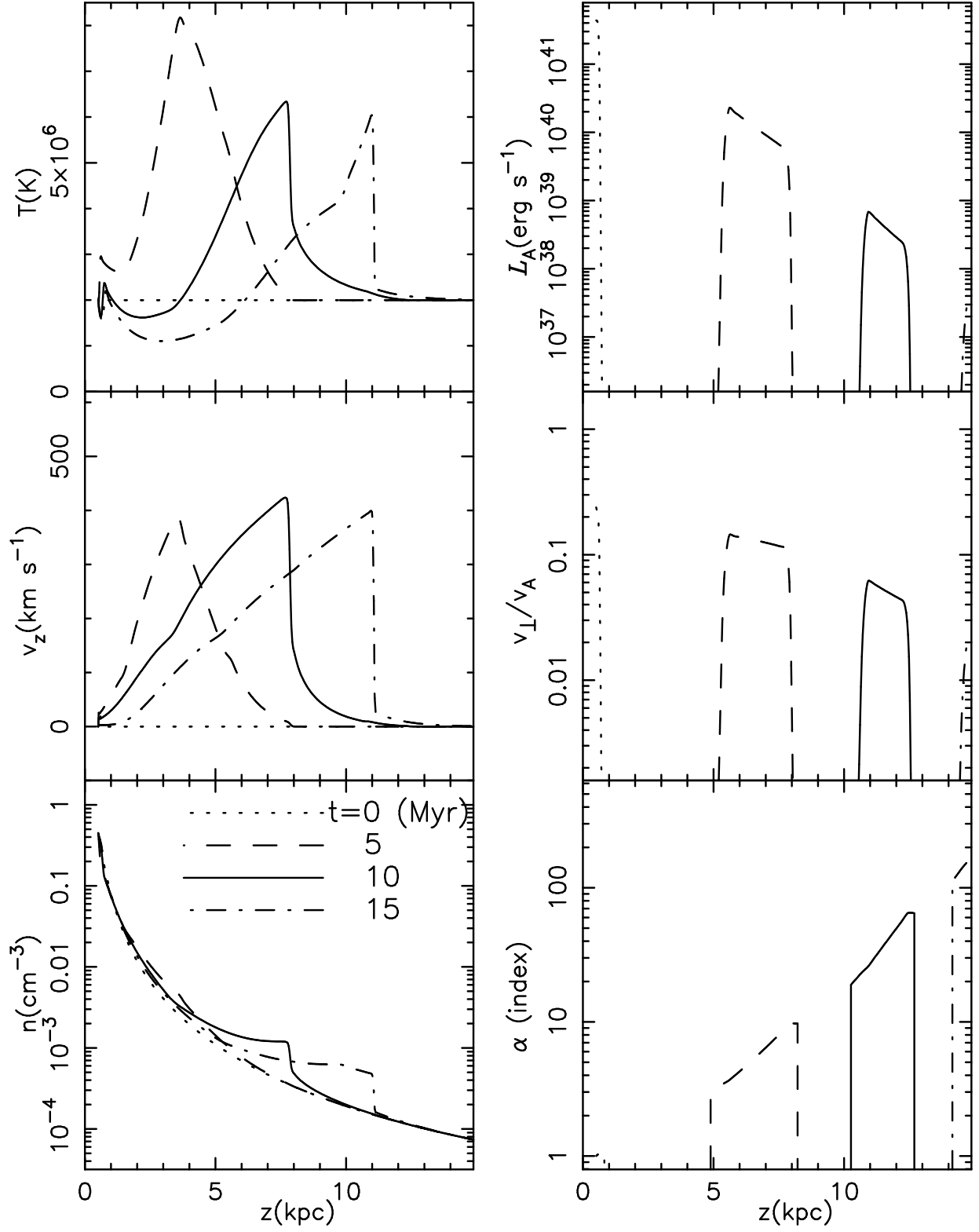


FIG. 6.— Time evolution of vertical distributions of physical quantities for the case with turbulent Mach number  $M_A = 0.5$  and injection time  $\tau_{\text{inj}} = 2$  Myr. Dotted, dashed, solid, and dot-dashed lines indicate  $t = 0, 5, 10,$  and  $15$  Myr, respectively. *Top Left:* Temperature,  $T$  (K). *Middle Left:* Vertical velocity,  $v_z$  ( $\text{km s}^{-1}$ ). *Bottom Left:* Particle number density,  $n$  ( $\text{cm}^{-3}$ ). *Top Right:* Alfvénic luminosity,  $L_A$  ( $\text{erg s}^{-1}$ ), described by Equation (31). *Middle Right:* Nonlinearity of the Alfvénic perturbations,  $v_{\perp}/v_A$ . *Bottom Right:* Spectral index,  $\alpha$ , of the Alfvénic perturbations. *Movie* is also available as a supplementary file and at <http://ea.c.u-tokyo.ac.jp/astro/Members/stakeru/research/movie/index.html>.

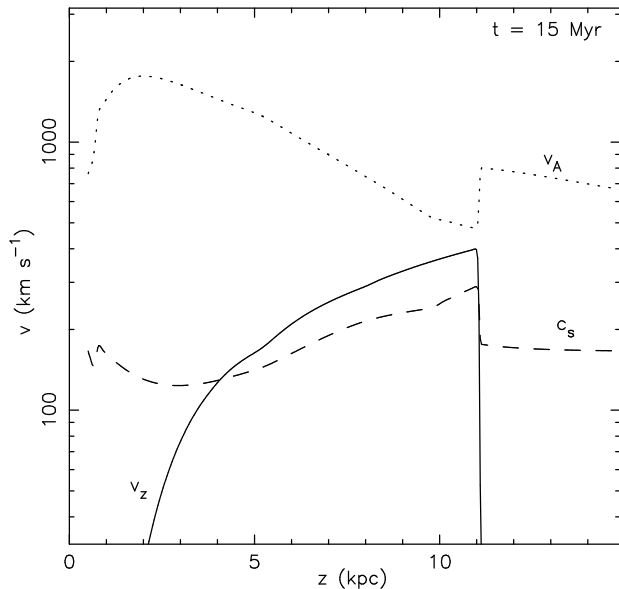


FIG. 7.— Comparison of vertical velocity,  $v_z$ , (solid), Alfvén speed,  $v_A$ , (dotted), and sound speed,  $c_s$ , (dashed) at  $t = 15$  Myr.

Injection Type	$\tau_{\text{inj}}$ (Myr)	$e_{A,0}$ (erg g $^{-1}$ )	$v_{\perp,0}$ (km s $^{-1}$ )
Continuous	20	$3.3 \times 10^{13}$	57
Temporal	2	$3.3 \times 10^{14}$	180

TABLE 1

PARAMETERS FOR THE INJECTED WAVE ENERGY.  $v_{\perp,0}$  IS DERIVED FROM  $e_{A,0}$  BY EQUATION (16).

1, the temperature is assumed to be locally isothermal with  $(2 - 5) \times 10^5$  K in the bulge region, which reflects the velocity dispersion of gas clouds. This temperature is lower than the temperature at the bottom boundary of the present model, and therefore, we adopt the lower density to give similar gas pressure ( $\propto nT$ ).

We inject Alfvénic perturbations by giving non-zero  $e_{A,0}$  from the bottom boundary, while the other variables,  $T$ ,  $v_z$ , and  $n$ , are fixed at the bottom boundary. At the outer boundary, we prescribe the outgoing condition by using equations for characteristics (Suzuki & Inutsuka 2005, 2006). We update  $\rho$ ,  $v_z$ ,  $T$  (or  $e_g$ ), and  $e_A$  by solving Equations (11) – (14) and Equation (19) during  $\tau_{\text{sim}} = 20$  Myr. We test two types of the energy injection: One is a continuous injection, in which  $e_{A,0}$  is constant throughout  $\tau_{\text{sim}}$ . The other is a temporal injection, in which we input  $e_{A,0} \neq 0$  during the initial  $t < \tau_{\text{inj}}$  and switch off  $e_{A,0}$  at  $t = \tau_{\text{inj}}$  to keep  $e_{A,0} = 0$  during  $\tau_{\text{inj}} < t < \tau_{\text{sim}}$ . The total injected energy is determined from the time-integrated  $L_A$  given by the 3D MHD simulation introduced in Section 2,

$$\rho v_A e_{A,0} \pi (R_{\text{out}}^2 - R_{\text{in}}^2) \tau_{\text{inj}} = L_A \tau_{\text{sim}}, \quad (30)$$

where we adopt  $L_A = 4.3 \times 10^{40}$  erg s $^{-1}$  (Figure 2). Table 1 summarizes  $e_{A,0}$  that satisfies Equation (30). Here, the velocity amplitude,  $v_{\perp,0}$ , is derived from Equation (16).

#### 4. RESULTS

Figure 6 presents how an outflow is driven by the injected Alfvénic Poynting flux in the case with  $M_A = 0.5$

and  $\tau_{\text{inj}} = 2$  Myr. We show the evolution of physical quantities of the gas in the left panels and physical properties of the Alfvénic waves in the right panels. The top right panel shows the quantity,

$$\mathcal{L}_A \equiv S_A A \pi (R_{\text{out}}^2 - R_{\text{in}}^2), \quad (31)$$

in units of luminosity (erg s $^{-1}$ ) for the comparison to Figures 2 & 3 in Section 2, where

$$S_A = \rho e_A \frac{(v_A + v_z)^2}{v_A} \quad (32)$$

is an adiabatic constant called wave action (Jacques 1977, see also Equation A10 in Appendix). We call  $\mathcal{L}_A$  “wave action luminosity” in this paper.

$\mathcal{L}_A$  decreases rapidly with  $z$ , and the nonlinearity,  $v_{\perp}/v_A$ , (middle right panel) is kept  $\lesssim 0.2$ , which justifies the linear damping process adopted here as a dominant mechanism. Because of the rapid damping of the Poynting flux, the gas is effectively heated up (top left panel). One can clearly see the formation of a shock front that moves upward. The temperature at the shock front reaches  $T = 8 \times 10^6$  K at  $t = 5$  Myr and  $T = 6 \times 10^6$  K at  $t = 10$  Myr. Accordingly, the gas is accelerated to  $v_z = 400 - 500$  km s $^{-1}$  (middle left panel). The shock heating also contributes to the mass loading to the upper layer, and the density increases to  $n \approx (6 - 7) \times 10^{-4}$  cm $^{-3}$  at  $z = 10$  kpc when the shock front passes there at  $t = 13.5$  Myr. These physical quantities are consistent with observationally derived values,  $T = (4 - 5) \times 10^6$  K and  $n \approx 10^{-3}$  cm $^{-3}$  introduced in Section 1 (Miller & Bregman 2016).

Comparing the top right panel to the left three panels in Figure 6, we may find that the front of the Alfvénic wave travels faster than the shock front because the Alfvén speed is higher than the sound speed, which is shown in Figure 7. On the other hand, we cannot find any signature in the hydrodynamical quantities,  $T$ ,  $v_z$ , and  $n$ , at the front of the Alfvénic wave. In this case with  $M_A = 0.5$ , the Poynting flux is damped at a lower altitude. Therefore, they cannot significantly contribute to the acceleration by the magnetic pressure with Alfvénic perturbations (Equation 12) at a higher altitude  $\gtrsim 5$  kpc, but simply heats up the gas by the dissipation of the Poynting flux below  $z < 5$  kpc.

The bottom right panel of Figure 6 shows that the spectral index,  $\alpha$ , increases as the Alfvénic waves propagate. This is because waves with higher  $\omega$  are damped more rapidly (see Equation 25)

Figure 7 shows that the outflow is supersonic ( $v_z > c_s$ ) but slightly sub-Alfvénic even at the shock front. However,  $v_z$  exceeds the local escape velocity  $\sim 100$  km s $^{-1}$  at  $z \approx 10$  kpc, and therefore, this outflow will not return back but further streams outward and escapes from the gravity of the Galaxy.

The Alfvén velocity,  $v_A (\propto B_z / \sqrt{n})$ , increases rapidly in  $z < 2$  kpc owing to the rapid drop of the density,  $n$ , there (see Figure 6). However, it gradually decreases because the effect of the decrease of  $B_z$  by the expansion of the magnetic flux tube (Equations 9 & 10) surpasses the effect of the decrease of  $n$ . The mass supply from the lower region additionally slows down the decrease of  $n$  with  $z$ . The profile of  $v_A$  is qualitatively similar to that obtained in the solar atmosphere (e.g., Verdini et al. 2012); the Alfvén velocity increases with height in the



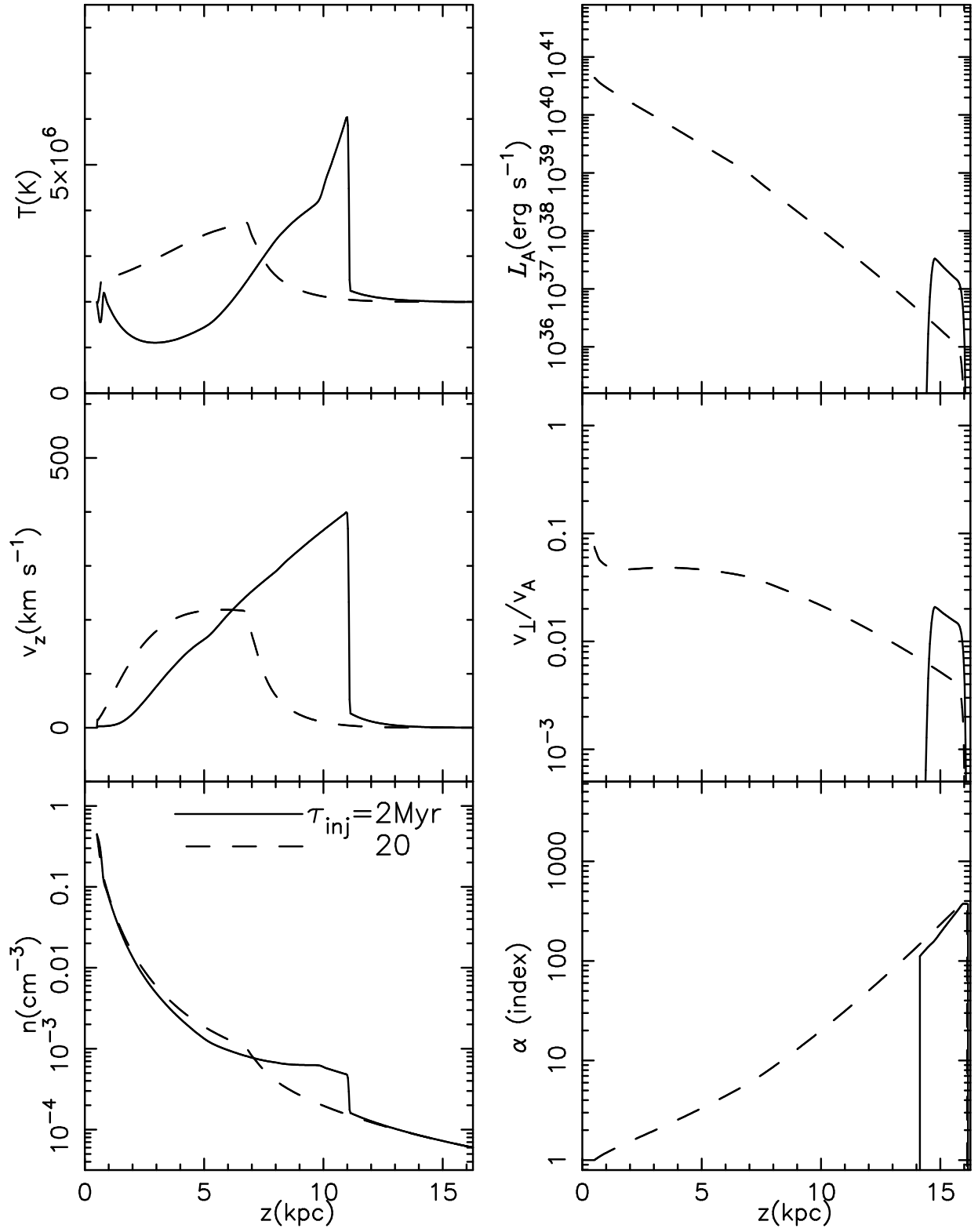


FIG. 8.— Comparison of cases with different  $\tau_{\text{inj}} = 2$  Myr (solid) and 20 Myr (dashed) for  $M_A = 0.5$  at  $t = 15$  Myr. The six panels are the same as in Figure 6.

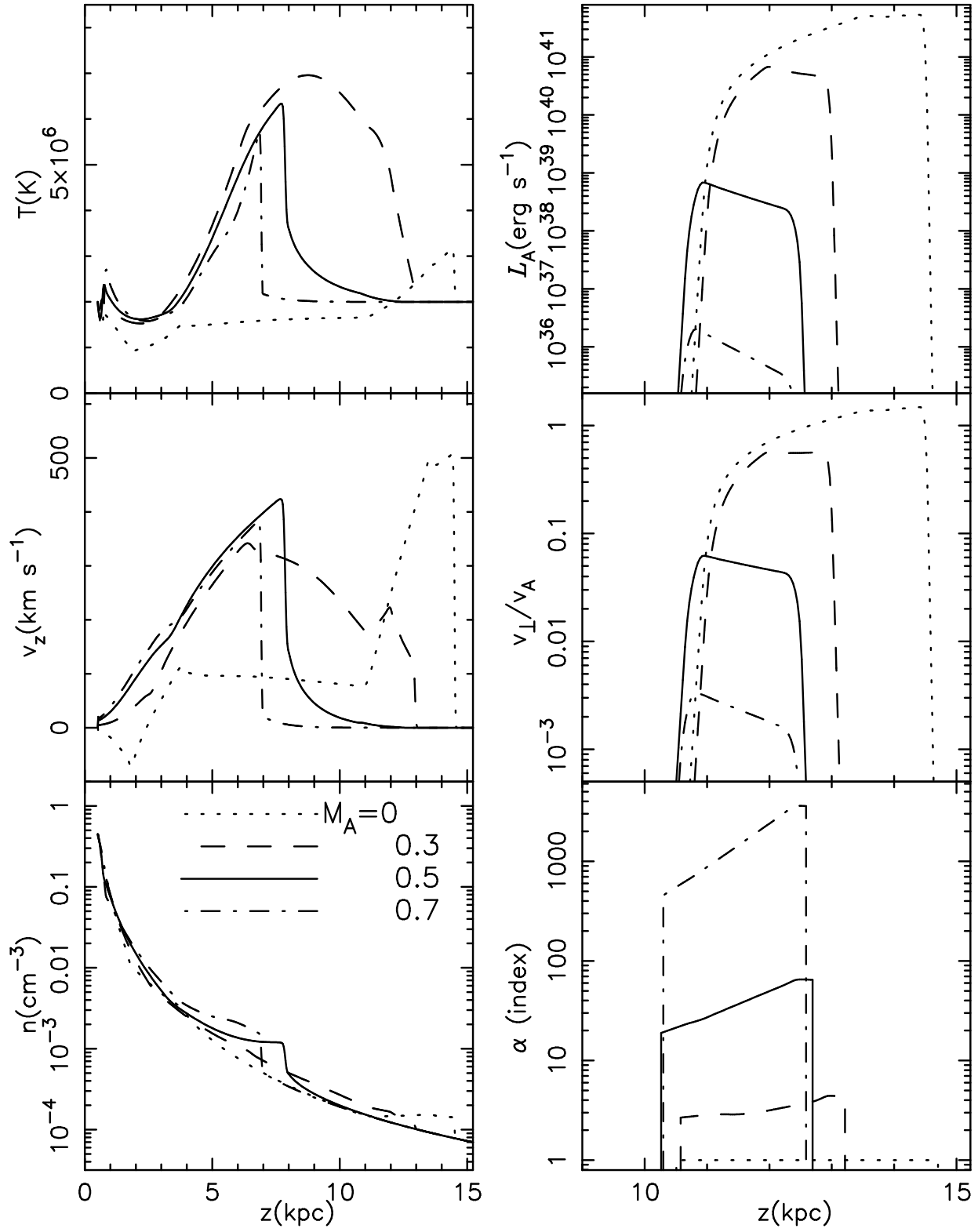


FIG. 9.— Comparison of cases with different  $M_A = 0$  (dotted), 0.3 (dashed), 0.5 (solid), and 0.7 (dot-dashed) for  $\tau_{\text{inj}} = 2$  Myr at  $t = 10$  Myr. The six panels are the same as in Figure 6.

corona because of the decrease of the density; however, it gradually decreases with height in the solar wind because the decrease of the density becomes gradual by the mass supply from the solar wind in addition to the decrease of the magnetic field strength.

We should note that the detailed profile of  $v_A$  in Figure 7 depends on the properties of the magnetic flux tube. If we adopt smaller  $B_{\text{mid}}$  and/or smaller  $z_{\text{break}}$ ,  $B_z$  and  $v_A$  at higher altitudes are reduced. In this case, the location of the wave dissipation is shifted to a lower altitude, namely it is equivalent to enhanced wave damping. In other words, a different choice of the magnetic flux tube is effectively replaced by a different choice of  $M_A$  that controls wave dissipation in our formulation. Therefore, we fix the parameters of the magnetic flux tube and focus on the dependence on  $M_A$  below.

Figure 8 compares two cases with different  $\tau_{\text{inj}}$  for a fixed  $M_A = 0.5$ . Since the total energies injected from the lower boundary are the same in the two cases, the input energy flux is smaller for the case with the longer injection,  $\tau_{\text{inj}} = 20$  Myr. This case also shows the formation of a shock wave, although its amplitude is smaller than in the temporal injection case ( $\tau_{\text{inj}} = 2$  Myr). The peak temperature and velocity are also lower for longer  $\tau_{\text{inj}}$ .

Figure 9 compares cases with different  $M_A$ , which directly controls the damping rate of the Poynting flux (Equation 25), for a fixed  $\tau_{\text{inj}} = 2$  Myr. In the no damping case ( $M_A = 0$ ) the Poynting flux does not contribute to the heating but transfer the only momentum to the gas; the heating of the gas is possible only by adiabatic compression. Hence, the temperature does not increase so much. On the other hand, the gas is accelerated mainly by the magnetic pressure to  $> 500$  km s $^{-1}$ .

The outflow structure of the case with  $M_A = 0.3$  shows intermediate properties between the case with  $M_A = 0.5$  and the case  $M_A = 0$ ; both energy (heating) and momentum (acceleration) transfers from the Poynting flux to the gas are important. Comparison of the middle-left ( $v_z$ ) panel to the right panels shows that the outflow is first led by the front of the injected Alfvénic flux. This illustrates that the initial upflow is driven directly by the magnetic pressure, which was not seen in the fast damping cases with  $M_A = 0.5$  and  $0.7$ . One can see that the initial  $v_z$  peak is followed by the second peak, which corresponds to the shock front seen in the fast damping cases, pushed by the gas pressure and travels with speed of  $\sim c_s$ . Therefore, we can understand that the initial front is created by the direct momentum transfer from the Poynting flux and the second peak is formed as a result of the heating by the wave dissipation.

The case with  $M_A = 0.3$  also shows that the gas is heated up to  $T = (6 - 7) \times 10^6$  K, which is comparable to the temperatures obtained in the case with  $M_A = 0.5$ . However, the density is not so high as that for  $M_A = 0.5$ , because the heating near the footpoint is weaker and sufficient mass loading is not achieved. The middle right panel shows that the nonlinearity is kept  $\approx 0.5$  even though the wave action luminosity decreases because of the wave damping. This is mainly because the Alfvén speed decreases by the expansion of the flux tube. In such circumstances, nonlinear damping processes (see Subsection 5.1) would efficiently work to suppress the nonlinearity. Therefore, in realistic situations, the wave

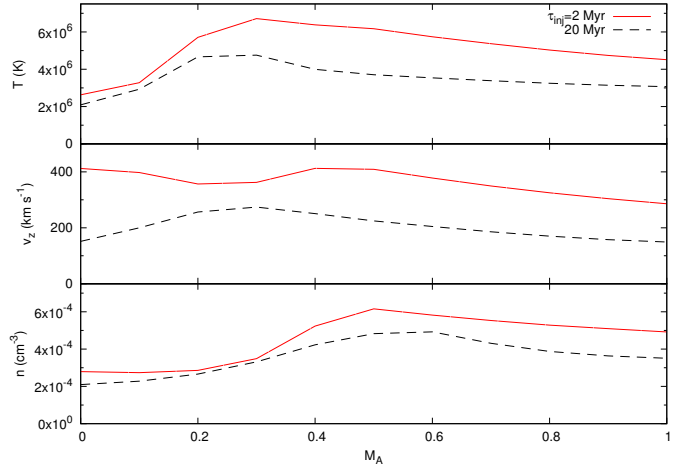


FIG. 10.— Dependence of the maximum temperature (top), vertical velocity (middle), and density (bottom) at  $z = 10$  kpc on  $M_A$ . Note that  $M_A$  determines the damping rate of the Poynting flux. Red solid and black dashed lines correspond to the cases for the temporal injection ( $\tau_{\text{inj}} = 2$  Myr) and the cases for the continuous injection ( $\tau_{\text{inj}} = 20$  Myr), respectively.

dissipation would be enhanced to further heat up the gas.

Figure 10 presents the maximum temperature, the maximum vertical velocity, and the maximum density measured at  $z = 10$  kpc for cases with different  $M_A$ . The top panel shows that the initial temperature ( $= 2 \times 10^6$  K) is kept for the no dissipation cases,  $M_A = 0$ . The maximum temperature  $\approx 7 \times 10^6$  K for  $\tau_{\text{inj}} = 2$  Myr and  $\approx 5 \times 10^6$  K for  $\tau_{\text{inj}} = 20$  Myr is obtained for moderately small dissipation,  $M_A \approx 0.3$ . This is because the heating is kept up to higher locations  $z \gtrsim 10$  kpc on account of the moderately slow dissipation of the Poynting flux.

The middle panel shows that the temporal injection ( $\tau_{\text{inj}} = 2$  Myr) cases give faster  $v_z \approx 300 - 400$  km s $^{-1}$  than the continuous injection ( $\tau_{\text{inj}} = 20$  Myr) cases as expected. The temporal cases shows a bimodal trend with two maximums of  $v_z$  at  $M_A = 0$  and  $0.4 - 0.5$ . The first peak at  $M_A = 0$  is from the outflow directly driven by the magnetic pressure of the Alfvénic Poynting flux, while the second peak at  $M_A = 0.4 - 0.5$  is from the outflow driven by the gas pressure (Figure 9).

The bottom panel shows a single maximum for  $n$  at  $M_A \approx 0.5 - 0.6$  in both cases with  $\tau_{\text{inj}} = 2$  and  $20$  Myr. This is qualitatively similar to the temperature (top panel), but the peak location is shifted to larger  $M_A$ , because sufficient heating by the wave dissipation near the footpoint is necessary to drive dense outflows (e.g., Lamers & Cassinelli 1999).

## 5. DISCUSSION

We have studied how outflows are driven by long-wavelength Alfvénic waves from magnetic activity in the bulge. In this section we discuss limitations regarding approximations we have assumed when handling the propagation and dissipation of the Alfvénic Poynting flux.

### 5.1. Nonlinear Effects

We considered turbulent damping for the main dissipation channel of the Alfvénic waves. This mechanism is essentially a linear process, and therefore it is dominant for waves for  $v_{\perp}/v_A \ll 1$ . Figure 9 shows that this

condition is satisfied for the cases with moderately large dissipation,  $M_A \geq 0.5$ . However, this is not the case for  $M_A \leq 0.3$  because the amplitude becomes  $v_\perp/v_A \gtrsim 0.5$  so that the Alfvén waves are nearly nonlinear. For these waves, nonlinear damping processes probably operate to enhance the dissipation.

For example, direct steepening of wave fronts occurs effectively. As a result, Alfvénic waves steepen to fast MHD shock trains and finally dissipate (Suzuki 2004). These are small-scale fast MHD shocklets and different from the large-scale hydrodynamical shock wave excited by the initial dissipation of the injected Alfvénic Poynting flux presented in Section 4 and Figures 6 & 9. However, they are also expected to contribute to the heating and driving hot outflows. In addition, longitudinal slow MHD waves are also excited by the fluctuating magnetic pressure of the Alfvénic waves (Matsumoto & Suzuki 2012, 2014; Miyamoto et al. 2014). These small-scale slow MHD ( $\approx$  acoustic) shocklets further contribute to the heating. This nonlinear mode conversion mechanism is also important in terms of the generation of density perturbation, which plays a role in the reflection of Alfvénic waves (Suzuki & Inutsuka 2006) as shown below.

Nonlinear interactions between different waves will be also efficient. In particular, the interaction between counter-propagating Alfvén waves as a result of reflection (see Section 5.2) excites MHD turbulence (e.g., Goldreich & Sridhar 1995; Cho & Lazarian 2003), which increases  $M_A$ . Although we have assumed that the Alfvén waves propagate in the turbulent media with a constant  $M_A$ , this argument shows that in reality propagating waves probably affect properties of the turbulence. Therefore, the wave amplitude and  $M_A$  of the background turbulence are regulated each other, which is to be pursued in future works.

### 5.2. Reflection

We treated the propagation of the Alfvénic waves, instead of directly solving wave equations, by updating energy  $e_A$  and the spectral index  $\alpha$  with time under the WKB approximation, which is satisfied under the condition that the wavelength is sufficiently smaller than the variation scale of the Alfvén speed. By this treatment, we could avoid numerical diffusion that particularly affects propagation of high-frequency (short-wavelength) waves. On the other hand, unless this condition is satisfied, Alfvén waves are reflected by the change of the wave shape (Suzuki & Inutsuka 2006; Shoda & Yokoyama 2016). We adopted the wide-band spectrum (Equation 17). The lower frequency boundary,  $\omega_0 = 1/1$  Myr corresponds to the longest wavelength we consider, which is an order of 1 kpc (Equation 29). The typical variation scale of  $v_A$  is comparable to 1 kpc in  $z \lesssim 2$  kpc, and moderately larger than 1 kpc in  $z \gtrsim 1$  kpc (Figure 7). Therefore, the Alfvén waves near  $\omega = \omega_0$  are ex-

pected to be subject to reflection at a low altitude. The reflected waves eventually interact with pre-existing up-going waves to excite Alfvénic turbulence as discussed in Section 5.1.

### 5.3. Other Sources

Although in this paper we only investigated the role of low-frequency Alfvénic Poynting flux with the period of 0.1 – 1 Myr, cosmic rays are believed to be a reliable candidate to drive large-scale outflows (Breitschwerdt et al. 1991; Everett et al. 2008); the effective pressure of the cosmic rays pushes the halo gas upward, and high-frequency Alfvén waves are excited via the streaming instability from the cosmic rays (Wentzel 1968). These waves are eventually damped by both nonlinear Landau process (Kulsrud & Pearce 1969; Beresnyak & Lazarian 2008) and MHD turbulence (Lazarian 2016), which plays a role in the heating of the gas.

These consecutive processes additionally contribute to accelerating and heating up the halo gas. In this sense, the results shown in the present paper give a lower bound for the temperature and velocity of the outflows.

## 6. SUMMARY & CONCLUSION

We studied roles of low-frequency Alfvénic waves with period of 0.1 – 1 Myr excited by magnetic activity, such as buoyantly rising magnetic loops and breakups of channel flows, in the Galactic bulge in driving large-scale outflows. We inspected the global 3D MHD simulation by Suzuki et al. (2015) and found that the time-averaged Alfvénic luminosity is  $10^{40} - 10^{41} \text{ erg s}^{-1}$ . We input this level of the Alfvénic Poynting flux from the footpoint of a magnetic flux tube that expands into the Galactic halo. We performed time-dependent hydrodynamic simulations with taking into account the propagation and dissipation of Alfvénic waves. We considered a linear dissipation mechanism of the Alfvénic waves in turbulent media developed by Yan & Lazarian (2002); Farmer & Goldreich (2004); Lazarian (2016).

Our model has essentially two parameters, the turbulent Mach number,  $M_A$ , that controls the dissipation of the Alfvénic waves, and the duration of the energy injection,  $\tau_{\text{inj}}$ . Our calculation shows that the basic thermal properties of the Fermi bubbles are well explained by cases with nearly transonic turbulence,  $M_A \approx 0.5$ , and an temporal injection,  $\tau_{\text{inj}} = 2$  Myr. This result shows that the magnetic activity in the Galactic bulge can potentially give a significant contribution to driving the Fermi-bubbles and large-scale outflows, although our treatment for the Alfvénic Poynting flux, which is a simplified one, need further elaboration in future studies.

This work was supported in part by Grants-in-Aid for Scientific Research from the MEXT of Japan, 17H01105 (TKS), and the NSF grants DMS 1622353 (AL). T.K.S. thanks Prof. Yasuo Fukui for fruitful discussion.

## APPENDIX

### DERIVATION OF WAVE ENERGY EQUATION AND WAVE ACTION

A general MHD expression of the total energy conservation is

$$\frac{\partial}{\partial t} \left[ \rho \left( \frac{v^2}{2} + e_g + \Phi \right) + \frac{B^2}{8\pi} \right] + \nabla \cdot \left[ \rho \mathbf{v} \left( \frac{v^2}{2} + e_g + p_g + \Phi \right) - \frac{1}{4\pi} (\mathbf{v} \times \mathbf{B}) \times \mathbf{B} \right] = 0. \quad (\text{A1})$$

Assuming 1D approximation along  $s$  coordinate ( $s = z$  in our calculations), Equation (A1) is rewritten as

$$\begin{aligned} \frac{\partial}{\partial t} \left[ \rho \left( \frac{v_s^2}{2} + e_g + \Phi \right) + \frac{B_s^2}{8\pi} + \frac{1}{2} \rho v_\perp^2 + \frac{B_\perp^2}{8\pi} \right] + \frac{1}{A} \frac{\partial}{\partial s} \left[ A \rho v_s \left( \frac{v_s^2}{2} + e_g + \frac{p_g}{\rho} + \Phi \right) \right. \\ \left. + A \left( \rho v_s \frac{v_\perp^2}{2} + \frac{1}{4\pi} v_s \mathbf{B}_\perp^2 - \frac{1}{4\pi} B_s \mathbf{v}_\perp \cdot \mathbf{B}_\perp \right) \right] = 0, \end{aligned} \quad (\text{A2})$$

where the subscript  $\perp$  indicates the two perpendicular components with respect to the  $s$  direction, and  $A$  is the cross section of a flux tube. If we consider Alfvénic perturbations that propagate along the  $+s$  ( $//B_s$ ) direction, the amplitudes of velocity and magnetic fields are related via

$$\mathbf{v}_\perp = -\frac{\mathbf{B}_\perp}{4\pi}. \quad (\text{A3})$$

Based on this relation, we define energy per mass,  $e_A$ , and energy flux,  $F_A$ , of Alfvénic perturbations:

$$e_A \equiv \frac{1}{2} \mathbf{v}_\perp^2 + \frac{B_\perp^2}{8\pi\rho} = \mathbf{v}_\perp^2 = \frac{B_\perp^2}{4\pi\rho}, \quad (\text{A4})$$

and

$$F_A = \frac{1}{2} \rho v_s \mathbf{v}_\perp^2 + \frac{1}{4\pi} v_s \mathbf{B}_\perp^2 - \frac{1}{4\pi} B_s \mathbf{v}_\perp \cdot \mathbf{B}_\perp = \rho e_A \left( \frac{3}{2} v_s + v_A \right), \quad (\text{A5})$$

where  $v_A = B_s / \sqrt{4\pi\rho}$ . Using  $e_A$ , Equation (A2) is further rewritten as

$$\frac{\partial}{\partial t} \left[ \rho \left( \frac{v_s^2}{2} + e_g + \Phi \right) + \frac{B_s^2}{8\pi} + \rho e_A \right] + \frac{1}{A} \frac{\partial}{\partial s} \left[ A \rho v_s \left( \frac{v_s^2}{2} + e_g + \frac{p_g}{\rho} + \Phi \right) + A \rho e_A \left( v_A + \frac{3}{2} v_s \right) \right] = 0. \quad (\text{A6})$$

Then, we can divide Equation (A2) into the Alfvénic part (Suzuki & Nagatani 2005; Suzuki et al. 2008),

$$\frac{\partial}{\partial t} (\rho e_A) + \frac{1}{A} \frac{\partial}{\partial s} \left[ A \rho e_A \left( v_A + \frac{3}{2} v_s \right) \right] - v_s \frac{\partial p_A}{\partial s} = -\gamma_A \rho e_A \quad (\text{A7})$$

and the hydrodynamic part,

$$\frac{\partial}{\partial t} \left[ \rho \left( \frac{v_s^2}{2} + e_g + \Phi \right) \right] + \frac{1}{A} \frac{\partial}{\partial s} \left[ A \rho v_s \left( \frac{v_s^2}{2} + e_g + \frac{p_g}{\rho} + \Phi \right) \right] + v_s \frac{\partial p_A}{\partial s} = \gamma_A \rho e_A, \quad (\text{A8})$$

where  $p_A = \frac{B_\perp^2}{8\pi} = \frac{1}{2} \rho e_A$  is the magnetic pressure associated with Alfvénic perturbations. When deriving Equation (A8), we use that  $B_s$  is constant with time in the 1D approximation. Equations (A7) and (A8) show that both components are connected by the momentum exchange through magnetic pressure ( $v_s \frac{\partial p_A}{\partial s}$ ) and the heating by the dissipation of Alfvénic perturbations ( $\gamma_A \rho e_A$ ). Readers may recognize that Equation (A7) is the first law of thermodynamics for Alfvénic perturbations; the energy density,  $\rho e_A$ , changes by the difference between the incoming and outgoing energy fluxes (2nd term on the left-hand side.), the work done on gas (3rd term on the left-hand side.) and dissipation (the right-hand side). Transforming the Eulerian form of Equation (A7) to the Lagrangian form, we get Equation (19), which we are solving in our calculations:

$$\rho \frac{de_A}{dt} + \frac{\partial}{\partial s} \left[ A \rho e_A \left( v_A + \frac{1}{2} v_s \right) \right] - v_s \frac{\partial p_A}{\partial s} = -\gamma_A \rho e_A \quad (\text{A9})$$

The second and third terms on the right-hand side of Equation (A7) can be combined to give (Jacques 1977)

$$\frac{\partial}{\partial t} (\rho e_A) + \frac{v_A}{v_A + v_s} \frac{1}{A} \frac{\partial}{\partial s} \left[ A \rho e_A \frac{(v_A + v_s)^2}{v_A} \right] = -\gamma_A \rho e_A. \quad (\text{A10})$$

This equation indicates that, for undamped ( $\gamma_A = 0$ ) Alfvén waves under time-steady condition ( $\frac{\partial}{\partial t} = 0$ ),  $\rho e_A \frac{(v_A + v_s)^2}{v_A}$  is an adiabatic constant, which is called wave action.

In this paper, we assume that waves with different wave frequencies evolve in an independent manner, and we can derive Equation (19) for wave energy density,  $\tilde{e}_A(\omega)$ , at  $\omega$ . In order to derive Equation (20), we here explicitly write an equation for  $\tilde{e}_A(\omega)$  by using Equation (17),

$$\rho \frac{d}{dt} (\tilde{e}_A(\omega_0) f(\omega/\omega_0)) + \frac{1}{A} \frac{\partial}{\partial z} \left[ A \rho \tilde{e}_A(\omega_0) f(\omega/\omega_0) \left( v_A + \frac{v_z}{2} \right) \right] - \frac{v_z}{2} \frac{\partial}{\partial z} [\rho \tilde{e}_A(\omega_0) f(\omega/\omega_0)] = -\gamma_A \rho \tilde{e}_A(\omega_0) f(\omega/\omega_0), \quad (\text{A11})$$

which is further transformed as

$$f(\omega/\omega_0) \left[ \rho \frac{d\tilde{e}_A(\omega_0)}{dt} + \frac{1}{A} \frac{\partial}{\partial z} \left\{ A \rho \tilde{e}_A(\omega_0) \left( v_A + \frac{1}{2} v_z \right) \right\} - \frac{v_z}{2} \frac{\partial}{\partial z} \{ \rho \tilde{e}_A(\omega_0) \} \right] + \rho \tilde{e}_A(\omega_0) \left[ \frac{d}{dt} f(\omega/\omega_0) + v_A \frac{\partial}{\partial z} f(\omega/\omega_0) \right]$$

$$= -\gamma_A \rho \tilde{e}_A(\omega_0) f(\omega/\omega_0). \quad (\text{A12})$$

We substitute the equation at  $\omega = \omega_0$ ,

$$\rho \frac{d\tilde{e}_A(\omega_0)}{dt} + \frac{1}{A} \frac{\partial}{\partial z} \left[ A \rho \tilde{e}_A(\omega_0) \left( v_A + \frac{1}{2} v_z \right) \right] - \frac{v_z}{2} \frac{\partial}{\partial z} \{ \rho \tilde{e}_A(\omega_0) \} = -\gamma_A \rho \tilde{e}_A(\omega_0), \quad (\text{A13})$$

into Equation (A12), and we obtain

$$\frac{d}{dt} f(\omega/\omega_0) + v_A \frac{\partial}{\partial z} f(\omega/\omega_0) = (\gamma_A(\omega_0) - \gamma_A(\omega)) f(\omega/\omega_0). \quad (\text{A14})$$

If  $f(\omega/\omega_0)$  has a power-law dependence, Equation (18), we can derive Equation (20).

#### REFERENCES

- Ackermann, M., Albert, A., Atwood, W. B., et al. 2014, *ApJ*, 793, 64
- Alazraki, G., & Couturier, P. 1971, *A&A*, 13, 380
- Balbus, S. A., & Hawley, J. F. 1991, *ApJ*, 376, 214
- Barkov, M. V., & Bosch-Ramon, V. 2014, *A&A*, 565, A65
- Belcher, J. W. 1971, *ApJ*, 168, 509
- Beresnyak, A., & Lazarian, A. 2008, *ApJ*, 678, 961
- Berkhuijsen, E. M., Haslam, C. G. T., & Salter, C. J. 1971, *A&A*, 14, 252
- Bland-Hawthorn, J., & Cohen, M. 2003, *ApJ*, 582, 246
- Bland-Hawthorn, J., Maloney, P. R., Sutherland, R. S., & Madsen, G. J. 2013, *ApJ*, 778, 58
- Breitschwerdt, D., McKenzie, J. F., & Voelk, H. J. 1991, *A&A*, 245, 79
- Carretti, E., Crocker, R. M., Staveley-Smith, L., et al. 2013, *Nature*, 493, 66
- Chandrasekhar, S. 1961, *Hydrodynamic and hydromagnetic stability* (Oxford: Clarendon)
- Chandrasekhar, S., & Fermi, E. 1953, *ApJ*, 118, 113
- Cheng, K. S., Chernyshov, D. O., Dogiel, V. A., & Ko, C. M. 2015, *ApJ*, 804, 135
- Cho, J., & Lazarian, A. 2003, *MNRAS*, 345, 325
- Crocker, R. M. 2012, *MNRAS*, 423, 3512
- Crocker, R. M., & Aharonian, F. 2011, *Physical Review Letters*, 106, 101102
- Crocker, R. M., Bicknell, G. V., Taylor, A. M., & Carretti, E. 2015, *ApJ*, 808, 107
- Crocker, R. M., Jones, D. I., Melia, F., Ott, J., & Protheroe, R. J. 2010, *Nature*, 463, 65
- Dobler, G., & Finkbeiner, D. P. 2008, *ApJ*, 680, 1222
- Dobler, G., Finkbeiner, D. P., Cholis, I., Slatyer, T., & Weiner, N. 2010, *ApJ*, 717, 825
- Egger, R. J., & Aschenbach, B. 1995, *A&A*, 294, L25
- Enokiya, R., Torii, K., Schultheis, M., et al. 2014, *ApJ*, 780, 72
- Everett, J. E., Zweibel, E. G., Benjamin, R. A., et al. 2008, *ApJ*, 674, 258
- Farmer, A. J., & Goldreich, P. 2004, *ApJ*, 604, 671
- Finkbeiner, D. P. 2004, *ApJ*, 614, 186
- Fujita, Y., Ohira, Y., & Yamazaki, R. 2013, *ApJ*, 775, L20
- Fukui, Y., Yamamoto, H., Fujishita, M., et al. 2006, *Science*, 314, 106
- Genzel, R., Eisenhauer, F., & Gillessen, S. 2010, *Reviews of Modern Physics*, 82, 3121
- Goldreich, P., & Sridhar, S. 1995, *ApJ*, 438, 763
- Guo, F., & Mathews, W. G. 2012, *ApJ*, 756, 181
- Inoue, T. 2012, *ApJ*, 760, 43
- Jacques, S. A. 1977, *ApJ*, 215, 942
- Kataoka, J., Tahara, M., Totani, T., et al. 2015, *ApJ*, 807, 77
- . 2013, *ApJ*, 779, 57
- Kopp, R. A., & Holzer, T. E. 1976, *Sol. Phys.*, 49, 43
- Koyama, K., Maeda, Y., Sonobe, T., et al. 1996, *PASJ*, 48, 249
- Kulsrud, R., & Pearce, W. P. 1969, *ApJ*, 156, 445
- Kuzio de Naray, R., McGaugh, S. S., & Mihos, J. C. 2009, *ApJ*, 692, 1321
- Lacki, B. C. 2014, *MNRAS*, 444, L39
- Lamers, H. J. G. L. M., & Cassinelli, J. P. 1999, *Introduction to Stellar Winds*, 452
- Lazarian, A. 2016, *ApJ*, 833, 131
- Machida, M., Nakamura, K. E., Kudoh, T., et al. 2013, *ApJ*, 764, 81
- Machida, M., Matsumoto, R., Nozawa, S., et al. 2009, *PASJ*, 61, 411
- Matsumoto, T., & Suzuki, T. K. 2012, *ApJ*, 749, 8
- . 2014, *MNRAS*, 440, 971
- Mertsch, P., & Sarkar, S. 2011, *Physical Review Letters*, 107, 091101
- Miller, M. J., & Bregman, J. N. 2016, *ApJ*, 829, 9
- Miyamoto, M., & Nagai, R. 1975, *PASJ*, 27, 533
- Miyamoto, M., Imamura, T., Tokumaru, M., et al. 2014, *ApJ*, 797, 51
- Mou, G., Yuan, F., Gan, Z., & Sun, M. 2015, *ApJ*, 811, 37
- Navarro, J. F., Frenk, C. S., & White, S. D. M. 1996, *ApJ*, 462, 563
- Parker, E. N. 1966, *ApJ*, 145, 811
- Pillai, T., Kauffmann, J., Tan, J. C., et al. 2015, *ApJ*, 799, 74
- Planck Collaboration, Ade, P. A. R., Aghanim, N., et al. 2013, *A&A*, 554, A139
- Ptuskin, V. S., Voelk, H. J., Zirakashvili, V. N., & Breitschwerdt, D. 1997, *A&A*, 321, 434
- Sano, T., Inutsuka, S., & Miyama, S. M. 1999, in *Astrophysics and Space Science Library*, Vol. 240, Numerical Astrophysics, ed. S. M. Miyama, K. Tomisaka, & T. Hanawa, 383
- Sasaki, K., Asano, K., & Terasawa, T. 2015, *ApJ*, 814, 93
- Shoda, M., & Yokoyama, T. 2016, *ApJ*, 820, 123
- Snowden, S. L., Egger, R., Freyberg, M. J., et al. 1997, *ApJ*, 485, 125
- Sofue, Y. 1977, *A&A*, 60, 327
- . 2000, *ApJ*, 540, 224
- . 2015, *PASJ*, 67, 75
- Sofue, Y., & Handa, T. 1984, *Nature*, 310, 568
- Su, M., Slatyer, T. R., & Finkbeiner, D. P. 2010, *ApJ*, 724, 1044
- Suzuki, T. K. 2004, *MNRAS*, 349, 1227
- Suzuki, T. K., Fukui, Y., Torii, K., Machida, M., & Matsumoto, R. 2015, *MNRAS*, 454, 3049
- Suzuki, T. K., & Inutsuka, S.-i. 2005, *ApJ*, 632, L49
- . 2006, *Journal of Geophysical Research (Space Physics)*, 111, 6101
- . 2009, *ApJ*, 691, L49
- . 2014, *ApJ*, 784, 121
- Suzuki, T. K., & Nagataki, S. 2005, *ApJ*, 628, 914
- Suzuki, T. K., Sumiyoshi, K., & Yamada, S. 2008, *ApJ*, 678, 1200
- Torii, K., Kudo, N., Fujishita, M., et al. 2010a, *PASJ*, 62, 1307
- . 2010b, *PASJ*, 62, 675
- Veilleux, S., Cecil, G., & Bland-Hawthorn, J. 2005, *ARA&A*, 43, 769
- Velikhov, E. P. 1959, *Zh. Eksp. Teor. Fiz.*, 36, 1398
- Verdini, A., Grappin, R., Pinto, R., & Velli, M. 2012, *ApJ*, 750, L33
- Vishniac, E. T., & Cho, J. 2001, *ApJ*, 550, 752
- Vishniac, E. T., & Shapovalov, D. 2014, *ApJ*, 780, 144
- Wentzel, D. G. 1968, *ApJ*, 152, 987
- Yan, H., & Lazarian, A. 2002, *Physical Review Letters*, 89, 281102
- Zirakashvili, V. N., Breitschwerdt, D., Ptuskin, V. S., & Voelk, H. J. 1996, *A&A*, 311, 113
- Zubovas, K., King, A. R., & Nayakshin, S. 2011, *MNRAS*, 415, L21